Spectrally pure visible-telecom photon pairs via dispersion-engineered Si_3N_4 waveguides

Vijay,[1] Shivani Sharma,[1] Joyee Ghosh,[1] and Vivek Venkataraman[1,2,*]

[1] *Department of Physics, Indian Institute of Technology Delhi, New Delhi 110016, India*
[2] *Department of Electrical Engineering, Indian Institute of Technology Delhi, New Delhi 110016, India*

(Received 5 October 2023; revised 10 April 2024; accepted 2 July 2024; published 26 July 2024)

We propose silicon nitride (Si_3N_4) nanowaveguide-based CMOS-compatible integrated sources of spectrally pure visible-telecom photon pairs. Our designs are intrinsically devoid of spectral correlations, eradicating the need for narrow-band filtering that reduces the source brightness. Further, the signal photons lie in the visible–near-infrared (vis-NIR) band, which can provide increased heralding efficiency of the idler photon in the telecom band using high-efficiency single-photon detectors. For example, a rectangular-cross-section silica-clad Si_3N_4 nanowaveguide with dimensions 680 nm × 840 nm and length 7 cm provides a heralded single-photon purity of approximately 91% for a pump wavelength of 956.8 nm and a pump bandwidth of 1200 GHz, with the signal and idler lying in the visible and telecom bands at approximately 701 nm and approximately 1505 nm, respectively, demonstrating a peak spectral brightness of approximately 1.2×10^4 photon pairs/s/nm/mW^2 for a linear propagation loss of 0.5 dB/cm. The effect of propagation losses on the purity is also studied for such source designs. We also propose some designs capable of generating high-purity photon pairs to address various specific vis-NIR quantum memory transitions with telecom-band interfacing for long-distance hybrid quantum networks. Such compact on-chip sources could have potential applications in various quantum technologies, such as sensing, simulation, computing, communication, and networking.

DOI: 10.1103/PhysRevApplied.22.014070

I. INTRODUCTION

Applications involving multiport quantum interferometers [1,2], such as sensing [3–5], simulation [6], computing [7,8], and repeaters [9,10], require the participating individual photons to be in spectrally pure states. The "mixedness" in the state of individual photons created by strong frequency correlations between photon pairs, typically generated either via $\chi^{(2)}$-based spontaneous parametric down-conversion (SPDC) [11,12] or via $\chi^{(3)}$-based spontaneous four-wave mixing (SFWM) [13,14], deteriorates the interference visibility, making them unfit for such quantum technology applications [15]. The traditionally employed solution to get rid of such frequency correlations involves narrow-band spectral filtering, resulting in a significant reduction of the output photon flux [16]. To overcome this limitation, intrinsically spectrally pure photon-pair sources at telecom using silicon-on-insulator (SOI) nanowaveguides [17], at NIR using periodically poled potassium titanyl phosphate (PPKTP) waveguides [18], and at visible-telecom using photonic crystal fibers [19] have been proposed or demonstrated by employing the technique of group-velocity matching (GVM) [15]. Recently, a CMOS-compatible on-chip source emitting spectrally pure visible-telecom photon pairs through a Si_3N_4 microring resonator has also been demonstrated [20]. This source offers discontinuous spectral tunability because of the azimuthal phase-matching condition (mode-number matching), via the input pump wavelength, the device geometry (requiring a good resolution in lithography), and the temperature (requiring additional experimental overheads). However, a CMOS-compatible source of intrinsically spectrally pure visible-telecom photon pairs offering continuous spectral tunability via the input pump wavelength has not yet been explored. Our proposed source provides this feature and is also tolerant toward fabrication inaccuracies. Such a source will have potential applications in efficiently generating heralded single photons at telecom wavelengths in a spectrally pure state as well as in addressing various vis-NIR quantum memories and linking them with telecom-band photons for long-distance hybrid (free-space plus fiber-optic) quantum networks. For applications involving heralded single photons, the quantum efficiency of heralding detectors is critical. The efficiency of room-temperature semiconductor-based single-photon detectors available at telecom wavelengths is low (approximately 20–30%) in comparison to those

---

[*] Contact author: vivekv@ee.iitd.ac.in

© 2024 American Physical Society

available at visible-NIR wavelengths (approximately 70–80%). Our integrated source designs are capable of generating signal photons in the visible-NIR band and idler photons in the telecom band, thus enabling the efficient generation of heralded single photons in the telecom band that can be transmitted over long distances via low-loss optical fibers.

Photon quantum memory is crucial for various quantum technology applications, including communication, computing, networking, and repeaters [21]. Different types of quantum memories have been demonstrated [22], such as those based on electromagnetically induced transparency (EIT) using rubidium (Rb) atoms (operating at 780 and 795 nm) or cesium (Cs) atoms (operating at 852 and 895 nm) [23], Raman quantum memories [24] using diamond (operating at 723 nm) [25], using rare-earth- (RE) doped crystals [26] with operating wavelengths corresponding to the RE elements, e.g., 793 nm for thulium, 880 nm for neodymium, and 1532 nm for erbium, and trapped-ion based quantum memories using ^{40}Ca ions at 854 nm [27–29]. The proposed designs are capable of generating high-spectral-purity photon pairs with one photon at the quantum memory transition and the other in the telecom band.

Silicon nitride is a third-order nonlinear material with a wide transparency window (approximately 0.4–3 μm) [30], low linear propagation losses (typically ≤ 1 dB/cm), negligible nonlinear losses such as two-photon absorption (TPA) and free-carrier absorption (FCA) [31], and a low thermo-optic coefficient (2.45×10^{-5} K^{-1}) [32], making it a good choice for designing high-performance integrated quantum light sources. Si$_3$N$_4$ has a considerable Kerr nonlinearity, with nonlinear index coefficient $n_{2,\mathrm{Si_3N_4}} \sim 2.6 \times 10^{-19}$ m^2/W [30], and provides sufficient refractive-index contrast between core ($n_{\mathrm{Si_3N_4}} \sim 2$) and cladding ($n_{\mathrm{SiO_2}} \sim 1.4$) to allow significant dispersion engineering for nonlinear photonics applications based on SFWM [33].

II. THEORY

Degenerate-pump spontaneous four-wave mixing (SFWM) is a third-order nonlinear process that generates two daughter photons called the signal and the idler at the frequency ω_s and ω_i, respectively, by annihilating two pump photons at frequency ω_p while conserving energy, $2\omega_p = \omega_s + \omega_i$ [34]. The phase mismatch for the degenerate-pump SFWM process (neglecting the nonlinear contribution for low input pump powers) is given by [35]

$$\Delta\beta = 2\beta_{\omega_p} - \beta_{\omega_s} - \beta_{\omega_i}, \tag{1}$$

where β_{ω_p}, β_{ω_s}, and β_{ω_i} are the propagation constants at the pump, signal, and idler frequencies, respectively. The propagation constant β, at a frequency ω_x, is given by $\beta(\omega_x) = \omega_x\, n_{\mathrm{eff}}(\omega_x)/c$, where $n_{\mathrm{eff}}(\omega_x)$ is the effective mode index at frequency ω_x. We are interested in discrete-band phase matching of signal and idler bands in order to satisfy the group-velocity-matching (GVM) condition required for spectral purity [17]. For a pulsed pump, Taylor expanding Eq. (1) around the central frequencies of pump (ω_{po}) and signal-idler ($\omega_{\mathrm{so}}/\omega_{\mathrm{io}}$) bands [15], the phase mismatch will become

$$\begin{aligned}\Delta\beta = {} & \Delta\beta^{(0)} + (\beta^{(1)}_{\omega_{po}} - \beta^{(1)}_{\omega_{\mathrm{so}}})\Delta\omega_s + (\beta^{(1)}_{\omega_{po}} - \beta^{(1)}_{\omega_{\mathrm{io}}})\Delta\omega_i \\ & + O_{\mathrm{II}}(\beta^{(2)}_{\omega_{po},\omega_{\mathrm{so}},\omega_{\mathrm{io}}}, \Delta\omega^2_{s,i}) + O_{\mathrm{III}}(\beta^{(3)}_{\omega_{po},\omega_{\mathrm{so}},\omega_{\mathrm{io}}}, \Delta\omega^3_{s,i}) \\ & + O_{\mathrm{IV}}(\beta^{(4)}_{\omega_{po},\omega_{\mathrm{so}},\omega_{\mathrm{io}}}, \Delta\omega^4_{s,i}) + O_{\mathrm{V}}(\beta^{(5)}_{\omega_{po},\omega_{\mathrm{so}},\omega_{\mathrm{io}}}, \Delta\omega^5_{s,i}),\end{aligned} \tag{2}$$

where $\Delta\beta^{(0)} = 2\beta_{\omega_{po}} - \beta_{\omega_{\mathrm{so}}} - \beta_{\omega_{\mathrm{io}}}$ is the zeroth-order phase mismatch, which will become zero for the phase-matched discrete bands. $\beta^{(n)}_{\omega_{xo}}$ is the nth-order dispersion at frequency ω_{xo}, given by $\beta^{(n)}_{\omega_{xo}} = (d^n\beta/d\omega^n)\big|_{\omega_{xo}}$ ($\beta^{(1)}_{\omega_{xo}}$ is the inverse group velocity at frequency ω_{xo}), $\Delta\omega_{s,i} = \omega_{s,i} - \omega_{\mathrm{so,io}}$ is the frequency detuning from the central frequencies of the signal-idler discrete band, $O_n(\beta^{(n)}_{\omega_{xo}}, \Delta\omega^n_{s,i})$ is the nth-order phase-mismatch term obtained from Taylor expansion of Eq. (1), which is a function of nth-order dispersion at the pump, signal, and idler central frequencies as well as the nth power of the signal and idler detunings, and the second and third terms in Eq. (2) represent first-order phase mismatch.

The wave function of an output two-photon state in a nonlinear parametric process, neglecting higher-order terms in the perturbative expansion [17], can be written as

$$|\psi(\omega_s,\omega_i)\rangle = K\int d\omega_s \int d\omega_i F(\omega_s,\omega_i)\hat{a}_s^\dagger(\omega_s)\hat{a}_i^\dagger(\omega_i)|\mathrm{vac}\rangle, \tag{3}$$

where K is a constant that depends on the input pump power P_p, the length of the waveguide L, and the effective nonlinearity γ. The operators $\hat{a}_s^\dagger(\omega_s)$ and $\hat{a}_i^\dagger(\omega_i)$ are the creation operators for the signal and idler modes, respectively, operating on the vacuum state $|\mathrm{vac}\rangle$. F(ω_s,ω_i) is the joint spectral amplitude (JSA), which specifies the signal-idler frequency correlations and is given by the product of the pump-envelope function (PEF) and the phase-matching function (PMF) [36]. The PEF, $\alpha(\omega_s,\omega_i)$, for the degenerate-pump configuration with a pump bandwidth σ_p, is expressed as [17]

$$\alpha(\omega_s,\omega_i) = \exp\frac{-(\Delta\omega_s + \Delta\omega_i)^2}{2\sigma_p^2} \tag{4}$$

and the PMF, $\phi(\omega_s, \omega_i)$, is given by

$$\phi(\omega_s,\omega_i) = \text{sinc}\left(\frac{\Delta\beta L}{2}\right)\exp\left(i\frac{\Delta\beta L}{2}\right), \tag{5}$$

where L is the waveguide length. A factorizable JSA, i.e., $F(\omega_s,\omega_i) = F_s(\omega_s)F_i(\omega_i)$, implies that the source lacks spectral correlations between the generated signal and idler photons [17]. The PEF is a straight line that lies in the ω_s-ω_i plane with a slope of −45°, with its width being proportional to the pump bandwidth σ_p. The PMF is a function of the phase mismatch $\Delta\beta$, given by Eq. (2), which in the first-order approximation also becomes a straight line, with a slope θ_{si} given by

$$\theta_{\text{si}} = -\tan^{-1}\left(\frac{\beta^{(1)}_{\omega_p}-\beta^{(1)}_{\omega_s}}{\beta^{(1)}_{\omega_p}-\beta^{(1)}_{\omega_i}}\right). \tag{6}$$

We use the approximation $\text{sinc}(x/2) \sim \exp(-rx^2)$ with $r = 0.048$ in Eq. (5), which leads to the following condition for the factorizability of joint spectral intensity (JSI = $|\text{JSA}|^2$) [15,37]:

$$\frac{1}{2\sigma_p^2} = -r\tau_s\tau_i, \tag{7}$$

where $\tau_{s/i} = (\beta^{(1)}_{\omega_p} - \beta^{(1)}_{\omega_s/\omega_i})L$ is the temporal lag between the pump and signal-idler photons at the output. It is clear from Eq. (7) that the source is devoid of correlations when τ_s and τ_i have opposite signs, i.e., the group velocity of the pump lies in between the group velocities of the signal and the idler. This condition of group-velocity matching in terms of the PMF angle θ_{si} [see Eq. (6)] demands that it should lie in the first quadrant, i.e., $0^\circ \leq \theta_{\text{si}} \leq 90^\circ$. With $\theta_{\text{si}} = 0^\circ$ and 90° (when the signal or idler group velocity is equal to the group velocity of the pump), the spectral correlations between the generated photons become a minimum and this condition is called asymmetric group-velocity matching (ASGVM). For $\theta_{\text{si}} = 45^\circ$, the group velocities of the signal and idler become equal and this condition is called symmetric group-velocity matching (SGVM). The heralded single-photon purity can be calculated numerically by the singular-value decomposition of the JSA and is defined as the inverse of the Schmidt mode number K [38], given by

$$K = \frac{1}{\Sigma_j \lambda_j^2}, \tag{8}$$

where the $\sqrt{\lambda_j}$s are the eigenvalues of the Schmidt decomposition of the JSA, i.e., $F(\omega_s,\omega_i) = \Sigma_j \sqrt{\lambda_j} f_{s,j}(\omega_s) f_{i,j}(\omega_i)$. The joint spectral intensity (JSI) given by $|F(\omega_s,\omega_i)|^2$ can be determined experimentally and can also be used to estimate the purity of the heralded single-photon state [39]. Although both the JSI and $\sqrt{\text{JSI}}$ lack the phase information, the latter, being close to the JSA, provides a better estimate of the actual spectral purity.

The flux of generated signal-idler photons Ω_p (photon pairs/s/Hz) or spectral brightness in the SFWM process [33,40] can be given by

$$\Omega_p = (\gamma P_p L)^2 e^{-\alpha L}\left|\frac{1-e^{-(\alpha+i\Delta\beta)L}}{(\alpha+i\Delta\beta)L}\right|^2, \tag{9}$$

where γ is the effective nonlinearity, α is the linear propagation loss, and P_p is the input pump power.

III. DISPERSION ENGINEERING

For the present study, we consider simple silica-clad Si_3N_4 waveguides with rectangular cross sections (see the inset in Fig. 1). These designs are optimized considering the phase matching for the fundamental TE mode, which is well confined with a mode area of approximately 0.3–0.9 μm^2 for the wavelengths of our interest, approximately 700–1730 nm. As per our objective, the discrete-band phase matching used to satisfy the required GVM condition for spectral purity should have one discrete band (the signal) at the visible-NIR wavelengths, while the other lies (the idler) in the telecom band. The phase mismatch for a waveguide width $w = 840$ nm, for three different heights h, is shown in Fig. 1 for 956.8-nm pump wavelength. The waveguide corresponding to a height $h = 610$ nm does not show any discrete bands. As the height increases to 680 nm, discrete bands start appearing in the visible and telecom regions at approximately 701 nm and approximately 1500 nm, respectively. With a further increase in height, the idler band shifts toward longer wavelengths and eventually leaves the telecom band of our interest. As a result, the optimum design that we

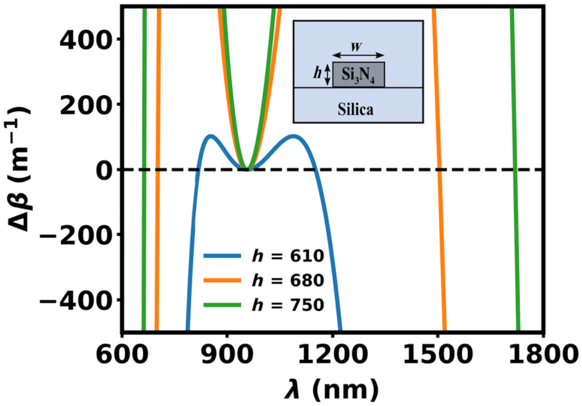

FIG. 1. The phase mismatch versus the signal-idler wavelength for three different waveguide heights h, shown in legend (in nanometers), corresponding to width $w = 840$ nm at an input pump wavelength of 956.8 nm. The inset shows the cross-section view of the silica-clad Si_3N_4 waveguide.

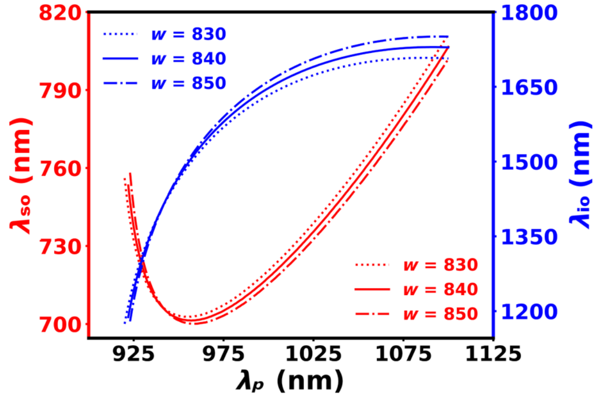

FIG. 2. The variation of the central wavelengths (corresponding to $\Delta\beta = 0$) of the signal (λ_{so}, left axis in red) and idler (λ_{io}, right axis in blue) discrete bands with the input pump wavelength λ_p for three different waveguide widths mentioned in the legend (in nanometers), each for a waveguide height of $h = 680$ nm.

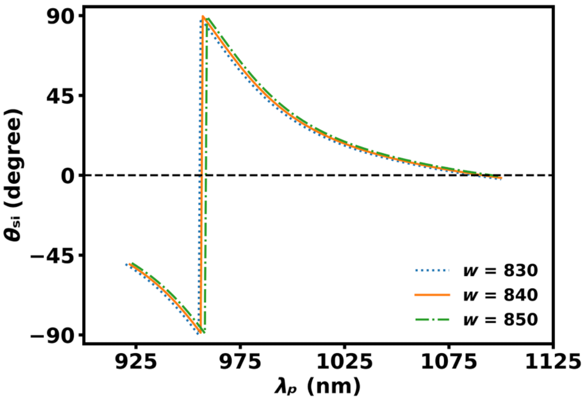

FIG. 3. The PMF angle θ_{si}, versus the input pump wavelength λ_p for three different waveguide widths (mentioned in the legend in nanometers) and a height of 680 nm. For width $w = 840$ nm, the transition from negative to positive θ_{si} happens at the pump wavelength of 956.8 nm, where θ_{si} reaches a maximum value of approximately 89.9°.

arrive at for generating the visible-telecom photon pairs is $h \times w = 680\ \mathrm{nm} \times 840\ \mathrm{nm}$.

In Fig. 2, we show the shift in the central wavelength of the signal-idler discrete bands with a change in input pump wavelength λ_p for three different waveguide widths (830, 840, and 850 nm) and a height of 680 nm, showing the tunability of the source. The wavelengths of the generated signal or idler photons for these three widths differ very slightly, showing the tolerance of our design toward changes in waveguide width due to fabrication errors. The pump-wavelength range that satisfies the GVM condition required for spectral purity, i.e., $0^\circ \leq \theta_{\mathrm{si}} \leq 90^\circ$, is approximately 957–1091 nm for the waveguide width 840 nm with θ_{si} being a maximum at approximately 957 nm and zero at approximately 1091 nm (see Fig. 3) (correspondingly, the signal and idler ranges are approximately 701–797 nm and approximately 1506–1729 nm, respectively). As is evident from Fig. 3, the variation in the PMF angle θ_{si} with the waveguide width is very small, which again shows the tolerance of our design toward fabrication errors in the waveguide width.

IV. SOURCE OPTIMIZATION

The spectral brightness given by Eq. (9) has been explored as a function of the waveguide length L, considering an exact phase-matching condition ($\Delta\beta = 0$). For the $h \times w = 680\ \mathrm{nm} \times 840\ \mathrm{nm}$ design, the spectral brightness calculated for two different linear propagation losses, $\alpha = 0.5$ and 2 dB/cm at an input pump power $P_p = 100$ mW, with an effective nonlinearity $\gamma \sim 3\ \mathrm{m}^{-1}\ \mathrm{W}^{-1}$, and effective mode area of approximately 0.57 $\mu\mathrm{m}^2$, is shown in Fig. 4. For a typical loss of 0.5 dB/cm, the spectral brightness saturates for a waveguide length $L \sim 7$ cm and decreases further with an increase in waveguide length due to propagation losses, as illustrated by the red curve ($\alpha = 2$ dB/cm) for the range of waveguide lengths in Fig. 4. Also, it is evident from Fig. 4 that the spectral brightness decreases with an increase in propagation losses. Since the photon purity also depends on the waveguide length L (explored next), accordingly, we can also choose slightly different waveguide lengths to facilitate high-purity photon generation by compromising spectral brightness.

As the PMF and PEF depend on the waveguide length L [Eq. (5)] and the input pump bandwidth σ_p [Eq. (4)], respectively, we can tune these two parameters to maximize the purity (derived from the JSA) at a particular pump wavelength λ_p (which determines the PMF angle θ_{si}). In Fig. 5, we show the purity of the photon pairs for the $h \times w = 680\ \mathrm{nm} \times 840\ \mathrm{nm}$ design, as a function of the pump

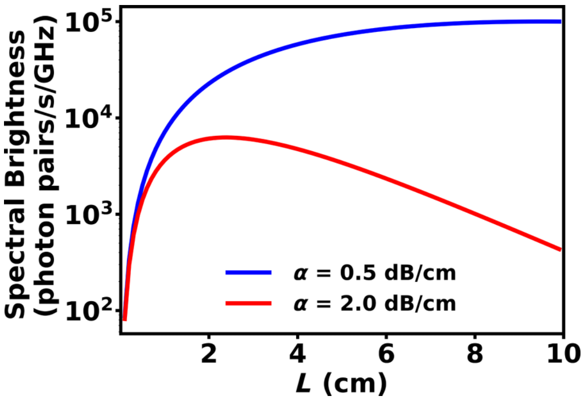

FIG. 4. The spectral brightness versus the waveguide length L for the $680\ \mathrm{nm} \times 840\ \mathrm{nm}$ design while pumping at 956.8 nm for two different linear propagation losses (mentioned in the legend) at an input pump power $P_p = 100$ mW, with an effective nonlinearity $\gamma \sim 3\ \mathrm{m}^{-1}\ \mathrm{W}^{-1}$ and an effective mode area of approximately 0.57 $\mu\mathrm{m}^2$.

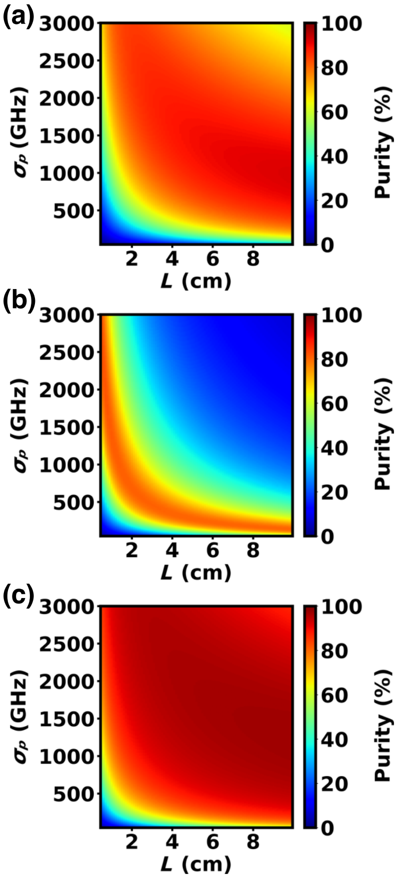

FIG. 5. The purity as a function of the pump bandwidth σ_p and the waveguide length L for the 680 nm × 840 nm design at (a) $\theta_{\text{si}} = 90^\circ$, corresponding to input pump wavelength $\lambda_p = 956.8$ nm, (b) $\theta_{\text{si}} = 45^\circ$, corresponding to input pump wavelength $\lambda_p = 987.55$ nm, and (c) $\theta_{\text{si}} = 0^\circ$, corresponding to input pump wavelength $\lambda_p = 1091.2$ nm.

bandwidth σ_p and the waveguide length L for three different PMF angles, 90° and 0° corresponding to ASGVM in Figs. 5(a) and 5(c), and 45° corresponding to SGVM in Fig. 5(b). The wavelength of the generated signal and idler photons at $\theta_{\text{si}} = 90^\circ$ (ASGVM) is 701.3 nm and 1505.2 nm, respectively, corresponding to an input pump wavelength of 956.8 nm (see Figs. 2 and 3). For $\theta_{\text{si}} = 45^\circ$ (SGVM), the signal and idler photon wavelengths are 710.7 nm and 1617.6 nm, respectively, at the input pump wavelength of 987.55 nm, and for $\theta_{\text{si}} = 0^\circ$ (ASGVM), the respective signal and idler wavelengths are 797 nm and 1729.7 nm at the input pump wavelength of 1091.2 nm.

For $\theta_{\text{si}} = 90^\circ$ [Fig. 5(a)], the purity is high ($\gtrsim 90\%$), for waveguide lengths of approximately 5.5–10 cm, with the corresponding optimum pump bandwidths being $\sigma_p \sim$ 650–1450 GHz. The required pump bandwidth for maximum purity decreases slightly with an increase in the waveguide length L [as expected from Eq. (7)]. For $L = 7$ cm, the maximum purity is approximately 91%, corresponding to $\sigma_p = 1200$ GHz (at input pump wavelength $\lambda_p = 956.8$ nm). For the SGVM case of $\theta_{\text{si}} = 45^\circ$ shown in Fig. 5(b), the region of maximum purity is narrower and shifted toward smaller pump bandwidths. For $L = 7$ cm, a maximum purity of approximately 80% is achieved with $\sigma_p = 200$ GHz (at input pump wavelength $\lambda_p = 987.55$ nm). Finally, for $\theta_{\text{si}} = 0^\circ$ (ASGVM), shown in Fig. 5(c), the high-purity region is even broader than that for $\theta_{\text{si}} = 90^\circ$ [Fig. 5(a)] with enhanced purity. The maximum purity is approximately 97%, again for $L = 7$ cm (the same waveguide can, in principle, be employed to achieve SGVM or any of the two ASGVM conditions simply by a change of pump wavelength) and $\sigma_p = 1500$ GHz (at input pump wavelength $\lambda_p = 1091.2$ nm).

In Fig. 6, the PEF, |PMF|, and the corresponding JSI are shown for the optimum $h \times w = 680$ nm × 840 nm design with $L = 7$ cm for (i) ASGVM with $\theta_{\text{si}} = 90^\circ$ and 0° in Figs. 6(a) and 6(c) respectively, and (ii) SGVM with $\theta_{\text{si}} = 45^\circ$ in Fig. 6(b). For ASGVM, the shape of the JSI is elliptical, with the major axis lying along the signal or idler axis corresponding to $\theta_{\text{si}} = 0^\circ$ or 90°, respectively, while for SGVM, the JSI is circular.

During the manufacture of photonic integrated circuits, departures from the targeted dimensions are unavoidable due to the limitations of the fabrication tools. The thickness of any dielectric layer (e.g., SiO_2 or Si_3N_4) during the growth process can be controlled with great accuracy [41] but, typically, the width of the waveguide can deviate considerably ($\geq$10 nm) from the targeted values during the lithography and etching processes [42]. In Fig. 7, we show the tolerance of our design, $h \times w = 680$ nm × 840 nm with $L = 7$ cm, toward such inaccuracies for the SGVM case, corresponding to the PMF angle $\theta_{\text{si}} = 45^\circ$. If the waveguide width deviates from the target value of 840 nm, we can accordingly tune the input pump wavelength λ_p to again facilitate signal-idler emission with a high purity of approximately 80%. This property of tolerance toward width inaccuracies of the proposed design is also demonstrated for the ASGVM case (not shown) of $\theta_{\text{si}} = 90^\circ$ and 0°, with a broader range of usable pump bandwidths corresponding to high purity, as is evident from Fig. 5.

The expected spectral brightness given by Eq. (9) per unit input pump power squared is also computed for our $h \times w = 680$ nm × 840 nm design (effective mode area of approximately 0.57 μm^2) and $L = 7$ cm, shown in Fig. 8. For a typical linear propagation loss of 0.5 dB/cm, the peak spectral brightness is approximately 1.2×10^4 photon pairs/s/nm/mW^2 at the signal wavelength of 701.3 nm [comparable to that of a photonic-crystal-fiber- (PCF) based source [19], and approximately $10^3 \times$ birefringent (PM) optical-fiber-based source [43]] for an input pump wavelength of 956.8 nm corresponding to the ASGVM condition ($\theta_{\text{si}} = 90^\circ$).

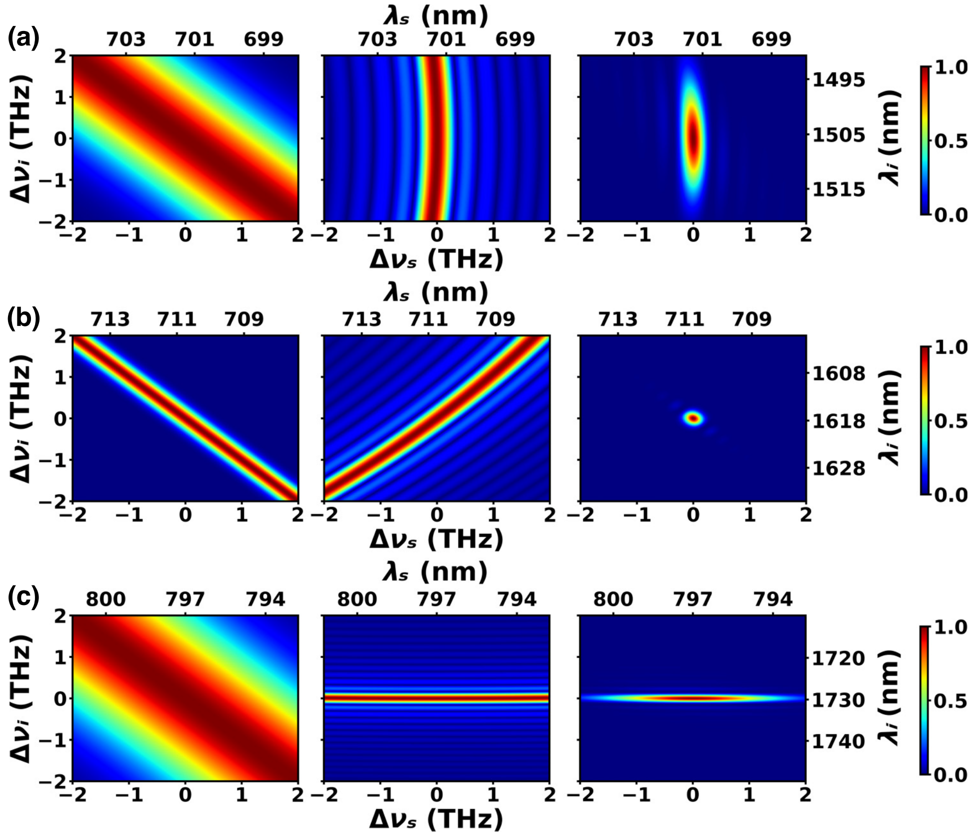

FIG. 6. The PEF, |PMF|, and JSI (from left to right) for the 680 nm × 840 nm design with a waveguide length $L = 7$ cm, corresponding to the PMF angle θ_{si}: (a) 90° at pump 956.8 nm with a bandwidth $\sigma_p = 1200$ GHz, yielding a purity of 91%, (b) 45° at pump 987.55 nm with a bandwidth $\sigma_p = 200$ GHz, yielding a purity of 80%, and (c) 0° at pump 1091.2 nm with a bandwidth $\sigma_p = 1500$ GHz, yielding a purity of 97%.

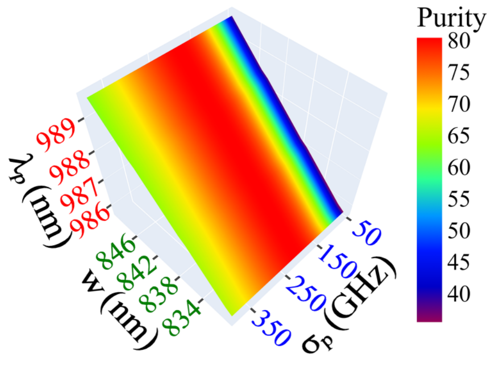

FIG. 7. The purity of the generated photon pairs as a function of the input pump bandwidth σ_p for the designs with a constant height $h = 680$ nm and different waveguide widths w, at the input pump wavelengths λ_p corresponding to SGVM, $\theta_{\mathrm{si}} = 45°$.

V. EFFECT OF LOSSES ON PURITY

As the photons travel through the Si_3N_4 waveguides, the losses experienced are mainly due to scattering caused by sidewall roughness [31,44]. The effect of such scattering losses on the heralded single-photon purity is explored for our designs. The modified JSA $F'(\omega_s, \omega_i)$ representing biphoton spectral correlations in the presence of losses [45,46] is given by

$$F'(\omega_s,\omega_i) = \alpha(\omega_s,\omega_i) \times e^{-\frac{\xi L}{2}} \times \frac{\mathrm{Sin}\left(\frac{\Delta\beta L}{2} - i\frac{\xi L}{2}\right)}{\frac{\Delta\beta L}{2} - i\frac{\xi L}{2}} \qquad (10)$$

where $\alpha(\omega_s, \omega_i)$ is the PEF given by Eq. (4), $\xi = (\alpha_s r_s + \alpha_i r_i - \alpha_p)/2$, α_p, α_s, and α_i are the propagation losses at the pump (ω_p), signal (ω_s), and idler (ω_i) frequencies, respectively, and $\mathrm{r}_{s/i} = \beta^{(1)}_{\omega_p}/\beta^{(1)}_{\omega_{s/i}}$ is the ratio of group velocities of the signal-idler and pump photons ($\beta^{(1)}_{\omega_x}$ is the inverse group velocity at frequency ω_x). For the optimum 680 nm × 840 nm design, the purity as a function of the propagation losses α ($= \alpha_p = \alpha_s = \alpha_i$) for three different PMF angles, $\theta_{\mathrm{si}} = 90°$, 45°, and 0°, is shown in Fig. 9, with a correspondingly exact input pump bandwidth σ_p and waveguide length L, as mentioned for Fig. 6. As is evident from Fig. 9, the photon purity decreases with an increase in the propagation loss α and the decrement is a maximum for $\theta_{\mathrm{si}} = 45°$, while it is a minimum for $\theta_{\mathrm{si}} = 0°$. This can be attributed to the fact that higher losses lead to a broadened

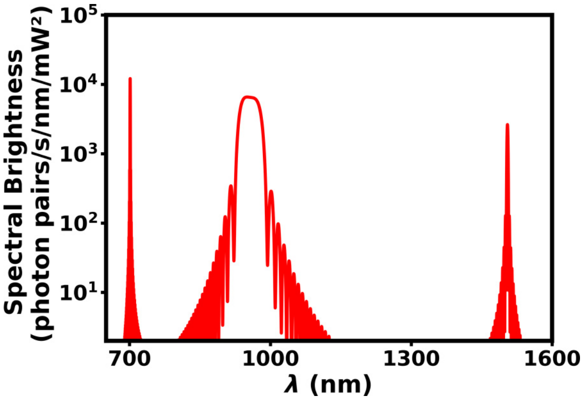

FIG. 8. The spectral brightness for the 680 nm × 840 nm design with a waveguide length $L = 7$ cm, an effective mode area of approximately 0.57 μm^2, and a linear propagation loss of 0.5 dB/cm, at the input pump wavelength of 956.8 nm (corresponding to $\theta_{\text{si}} = 90^\circ$). The peak spectral brightness at the generated signal-photon wavelength of 701.3 nm is 1.2×10^4 photon pairs/s/nm/mW^2.

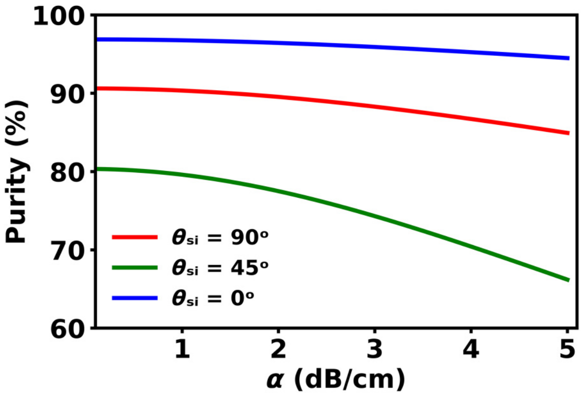

FIG. 9. The purity as a function of the propagation loss α $(= \alpha_p = \alpha_s = \alpha_i)$, for the 680 nm × 840 nm design with a waveguide length $L = 7$ cm, corresponding to three different PMF angles (mentioned in the legend), $\theta_{\text{si}} = 90^\circ$ with input pump wavelength $\lambda_p = 956.8$ nm and pump bandwidth $\sigma_p = 1200$ GHz, 45° with $\lambda_p = 987.55$ nm and $\sigma_p = 200$ GHz, and 0° with $\lambda_p = 1091.2$ nm and $\sigma_p = 1500$ GHz. As the loss increases from zero to 5 dB/cm, the purity drops to approximately 85% for $\theta_{\text{si}} = 90^\circ$, approximately 66% for $\theta_{\text{si}} = 45^\circ$, and approximately 94% for $\theta_{\text{si}} = 0^\circ$, respectively, from approximately 91%, 80%, and 97%, respectively.

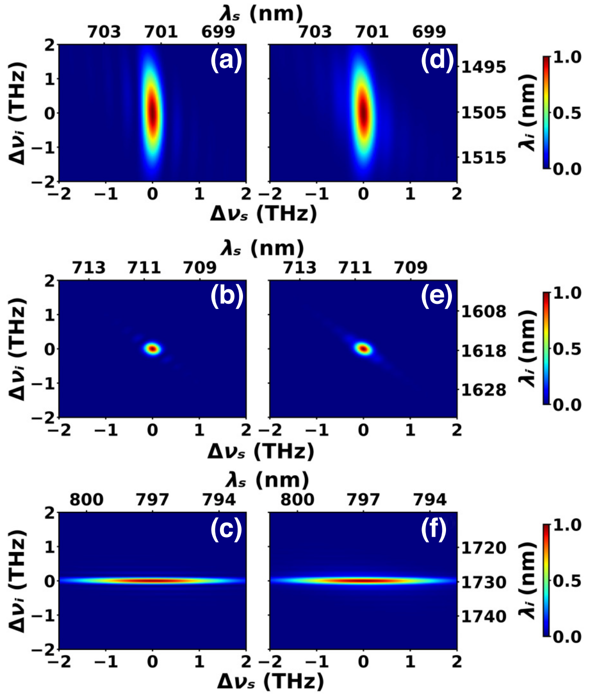

FIG. 10. The JSI for the 680 nm × 840 nm design with a waveguide length $L = 7$ cm for two different linear propagation losses: (a)–(c) $\alpha_{p,s,i} = 0.5$ dB/cm; (d)–(f) 5 dB/cm. Parts (a) and (d) correspond to PMF angles $\theta_{\text{si}} = 90^\circ$ with $\lambda_p = 956.8$ nm and $\sigma_p = 1200$ GHz, yielding purities of 91% and 85%, respectively; (b) and (e) correspond to $\theta_{\text{si}} = 45^\circ$ with $\lambda_p = 987.55$ nm, $\sigma_p = 200$ GHz, yielding purities of 80% and 66%, respectively; and (c) and (f) correspond to $\theta_{\text{si}} = 0^\circ$ with $\lambda_p = 1091.2$ nm, $\sigma_p = 1500$ GHz, yielding purities of 97% and 94%, respectively.

JSI, resulting in increased frequency correlations between the generated signal-idler; see Fig. 10, which shows the JSI for two different losses, $\alpha = 0.5$ [Figs. 10(a)–10(c)] and 5 dB/cm [Figs. 10(d)–10(f)]. Since there is no considerable effect on the purity for typical experimentally reported losses [31,44] for such designs, we can safely exclude the losses from the purity calculation. A recent demonstration of a heralded single-photon source based on silicon at telecom wavelengths has also reported a very high purity of approximately 99% for such loss values [47]. However, for higher propagation losses, the consideration of losses becomes essential. Also, the probability of successfully heralding a single photon at the output decreases with increased losses because of the possibility of losing one photon out of a pair [46].

VI. DISCUSSION

In the preceding sections, we have shown that a simple Si_3N_4 nanowaveguide design with a rectangular cross section of 680 nm × 840 nm is capable of generating spectrally uncorrelated photon pairs with high purity (up to approximately 97%) connecting the visible-NIR and telecom bands, the wavelength of emission of which can be tuned via the input pump wavelength. With a slightly higher thickness, $h = 730$ nm, and a smaller width of 810 nm, we can obtain the generated signal and idler photons at 674.3 nm and 1558.8 nm, respectively, while pumping with a pump at wavelength of 941.4 nm and a bandwidth of 1000 GHz, yielding a purity of approximately 92%, corresponding to a PMF angle of 90°.

Such devices could prove to be advantageous in several quantum technological applications, such as

TABLE I. The optimum designs, 660 nm × 800 nm and 600 nm × 1020 nm, with waveguide length $L = 7$ cm, capable of generating high-purity photon pairs for addressing various quantum memory transitions [the respective signal (λ_s) or idler (λ_i) wavelengths are in italics] by tuning the input pump wavelength λ_p and bandwidth σ_p.

λ_p (nm)	λ_s (nm)	λ_i (nm)	θ_{si} (°)	σ_p (GHz)	Purity (%)
660 nm × 800 nm					
1040.3	*780* (Rb D_2 line)	1561.35	8	400	86
1053	*793* (Tm^{+3}-doped crystal)	1566.65	4	550	89
1054.9	*795* (Rb D_1 line)	1567.27	3.5	620	90
1009.1	752.32	*1532* (Er^{+3}-doped crystal)	23	250	81
600 nm × 1020 nm					
1103.3	*852* (Cs D_2 line)	1564.86	17	600	82
1105.4	*854* ($^{40}\mathrm{Ca}^{+}$ ion)	1566.56	15.5	600	83
1130.6	*880* (Nd^{+3}-doped crystal)	1580.76	4	1150	89
1143.4	*895* (Cs D_1 line)	1582.65	0.2	2000	93

communication, networking, and computing [22,48]. For example, the majority of the demonstrated quantum memories, such as those based on EIT in atomic systems or with RE-ion-doped crystals, operate at vis-NIR wavelengths and connecting them with telecom wavelength photons propagating through the low-loss optical fiber network will extend the range of such distributed quantum protocols. Our designs are capable of addressing several specific quantum memories with high-purity photon pairs having the signal at respective atomic transition lines and the idler in the telecom band (or vis-NIR for the Er^{+3} quantum memory working at 1532 nm), by tuning the input pump wavelength λ_p and bandwidth σ_p. Table I summarizes two such designs, $h \times w = 660$ nm × 800 nm and 600 nm × 1020 nm (the waveguide length is 7 cm for both the designs) that can address many of the quantum memories reported so far [22,23]. These designs also show tolerance toward fabrication inaccuracies and we can compensate for any deviation from targeted widths by tuning the input pump wavelength λ_p as shown in Sec. IV. As the generated photon bandwidths from our proposed sources (approximately hundreds of gigahertz) are quite broad, addressing quantum memory transitions with narrow line widths ($\lesssim$10 GHz) will require further spectral filtering at the output but with the added advantage of increased photon-state purity [16]. Interestingly, we can also directly obtain such narrow-generation bandwidths with longer waveguide lengths, which will correspondingly require smaller input pump bandwidths for high purity. For example, the $h \times w = 660$ nm × 800 nm design can generate high-purity ($\gtrsim$82%) photon pairs with a narrow bandwidth of <10 GHz at all four quantum memory transitions listed in Table I, for a waveguide length $L = 3$ m and input pump bandwidth $\sigma_p = 6.5$ GHz. Spirally wound $\mathrm{Si_3N_4}$ waveguides with such long lengths have already been demonstrated experimentally, with record minimum propagation losses of $\leq$1.5 dB/m [49–51]. Further, such low propagation losses of approximately 2 dB/m and long lengths of approximately 3 m will boost the spectral brightness to approximately 10^8 photon pairs/s/nm/mW^2, becoming comparable to state-of-the-art $\chi^{(2)}$-based SPDC sources [52,53].

VII. CONCLUSIONS

In this paper, we propose silica-clad $\mathrm{Si_3N_4}$ waveguide designs capable of generating intrinsically (filter-free) spectrally pure visible-telecom photon pairs via SFWM. The simultaneous conditions of discrete-band phase matching and group-velocity matching required for spectral purity are achieved through dispersion engineering. The numerical results show that a design with cross section 680 nm × 840 nm can generate spectrally pure photon pairs with a maximum purity of up to approximately 97%, bridging the vis-NIR and telecom bands, the wavelengths of which can be tuned by the input pump wavelength, showing the tunability of our sources. Some other source designs, such as 660 nm × 800 nm and 600 nm × 1020 nm, are capable of generating high-purity photon pairs for addressing various quantum memory transitions with telecom-band interfacing. The proposed source designs also show tolerance toward the fabrication inaccuracies. The effect of waveguide propagation losses on purity is also explored and it is found that the purity remains unaffected for typical losses in such devices. The proposed sources could potentially be employed in various photonic quantum technologies, such as computing, simulation, communication, networking, and metrology.

ACKNOWLEDGMENTS

Vijay acknowledges the fellowship from the Ministry of Education, Government of India, under the Prime Minister Research Fellowship (PMRF) scheme.

[1] B. J. Metcalf, N. Thomas-Peter, J. B. Spring, D. Kundys, M. A. Broome, P. C. Humphreys, X.-M. Jin, M. Barbieri, W.

Steven Kolthammer, J. C. Gates, *et al.*, Multiphoton quantum interference in a multiport integrated photonic device, Nat. Commun. **4**, 1356 (2013).

[2] J. Wang, F. Sciarrino, A. Laing, and M. G. Thompson, Integrated photonic quantum technologies, Nat. Photonics **14**, 273 (2020).

[3] S. D. Huver, C. F. Wildfeuer, and J. P. Dowling, Entangled Fock states for robust quantum optical metrology, imaging, and sensing, Phys. Rev. A **78**, 063828 (2008).

[4] S. Zaiser, T. Rendler, I. Jakobi, T. Wolf, S.-Y. Lee, S. Wagner, V. Bergholm, T. Schulte-Herbrüggen, P. Neumann, and J. Wrachtrup, Enhancing quantum sensing sensitivity by a quantum memory, Nat. Commun. **7**, 12279 (2016).

[5] S. Pirandola, B. R. Bardhan, T. Gehring, C. Weedbrook, and S. Lloyd, Advances in photonic quantum sensing, Nat. Photonics **12**, 724 (2018).

[6] A. Aspuru-Guzik and P. Walther, Photonic quantum simulators, Nat. Phys. **8**, 285 (2012).

[7] P. Kok, W. J. Munro, K. Nemoto, T. C. Ralph, J. P. Dowling, and G. J. Milburn, Linear optical quantum computing with photonic qubits, Rev. Mod. Phys. **79**, 135 (2007).

[8] C. Taballione, T. A. Wolterink, J. Lugani, A. Eckstein, B. A. Bell, R. Grootjans, I. Visscher, D. Geskus, C. G. Roeloffzen, J. J. Renema, *et al.*, 8× 8 reconfigurable quantum photonic processor based on silicon nitride waveguides, Opt. Express **27**, 26842 (2019).

[9] K. Azuma, K. Tamaki, and H.-K. Lo, All-photonic quantum repeaters, Nat. Commun. **6**, 6787 (2015).

[10] W. J. Munro, K. Azuma, K. Tamaki, and K. Nemoto, Inside quantum repeaters, IEEE J. Sel. Top. Quantum Electron. **21**, 78 (2015).

[11] M. Fedorov, Y. M. Mikhailova, and P. Volkov, Gaussian modelling and Schmidt modes of SPDC biphoton states, J. Phys. B: At., Mol. Opt. Phys. **42**, 175503 (2009).

[12] M. Fiorentino, S. M. Spillane, R. G. Beausoleil, T. D. Roberts, P. Battle, and M. W. Munro, Spontaneous parametric down-conversion in periodically poled KTP waveguides and bulk crystals, Opt. Express **15**, 7479 (2007).

[13] B. Fang, O. Cohen, J. B. Moreno, and V. O. Lorenz, State engineering of photon pairs produced through dual-pump spontaneous four-wave mixing, Opt. Express **21**, 2707 (2013).

[14] R. L. Espinola, J. I. Dadap, R. M. Osgood, S. J. McNab, and Y. A. Vlasov, C-band wavelength conversion in silicon photonic wire waveguides, Opt. Express **13**, 4341 (2005).

[15] W. P. Grice, A. B. U'Ren, and I. A. Walmsley, Eliminating frequency and space-time correlations in multiphoton states, Phys. Rev. A **64**, 063815 (2001).

[16] E. Meyer-Scott, N. Montaut, J. Tiedau, L. Sansoni, H. Herrmann, T. J. Bartley, and C. Silberhorn, Limits on the heralding efficiencies and spectral purities of spectrally filtered single photons from photon-pair sources, Phys. Rev. A **95**, 061803 (2017).

[17] S. Sharma, V. Venkataraman, and J. Ghosh, Spectrally-pure integrated telecom-band photon sources in silicon, J. Lightwave Technol. **40**, 7529 (2022).

[18] C. Chen, J. E. Heyes, K.-H. Hong, M. Y. Niu, A. E. Lita, T. Gerrits, S. W. Nam, J. H. Shapiro, and F. N. Wong, Indistinguishable single-mode photons from spectrally engineered biphotons, Opt. Express **27**, 11626 (2019).

[19] C. Söller, B. Brecht, P. J. Mosley, L. Y. Zang, A. Podlipensky, N. Y. Joly, P. S. J. Russell, and C. Silberhorn, Bridging visible and telecom wavelengths with a single-mode broadband photon pair source, Phys. Rev. A **81**, 031801 (2010).

[20] X. Lu, Q. Li, D. A. Westly, G. Moille, A. Singh, V. Anant, and K. Srinivasan, Chip-integrated visible-telecom entangled photon pair source for quantum communication, Nat. Phys. **15**, 373 (2019).

[21] K. Heshami, D. G. England, P. C. Humphreys, P. J. Bustard, V. M. Acosta, J. Nunn, and B. J. Sussman, Quantum memories: Emerging applications and recent advances, J. Mod. Opt. **63**, 2005 (2016).

[22] F. Bussieres, N. Sangouard, M. Afzelius, H. De Riedmatten, C. Simon, and W. Tittel, Prospective applications of optical quantum memories, J. Mod. Opt. **60**, 1519 (2013).

[23] L. Ma, O. Slattery, and X. Tang, Optical quantum memory based on electromagnetically induced transparency, J. Opt. **19**, 043001 (2017).

[24] A. Kozhekin, K. Mølmer, and E. Polzik, Quantum memory for light, Phys. Rev. A **62**, 033809 (2000).

[25] D. G. England, K. A. Fisher, J.-P. W. MacLean, P. J. Bustard, R. Lausten, K. J. Resch, and B. J. Sussman, Storage and retrieval of THz-bandwidth single photons using a room-temperature diamond quantum memory, Phys. Rev. Lett. **114**, 053602 (2015).

[26] M. Guo, S. Liu, W. Sun, M. Ren, F. Wang, and M. Zhong, Rare-earth quantum memories: The experimental status quo, Front. Phys. **18**, 21303 (2023).

[27] N. Piro, F. Rohde, C. Schuck, M. Almendros, J. Huwer, J. Ghosh, A. Haase, M. Hennrich, F. Dubin, and J. Eschner, Heralded single-photon absorption by a single atom, Nat. Phys. **7**, 17 (2011).

[28] J. Huwer, J. Ghosh, N. Piro, M. Schug, F. Dubin, and J. Eschner, Photon entanglement detection by a single atom, New J. Phys. **15**, 025033 (2013).

[29] E. Arenskötter, T. Bauer, S. Kucera, M. Bock, J. Eschner, and C. Becher, Telecom quantum photonic interface for a $^{40}Ca^+$ single-ion quantum memory, npj Quantum Inf. **9**, 34 (2023).

[30] Y. Hong, Y. Hong, J. Hong, and G.-W. Lu, Dispersion optimization of silicon nitride waveguides for efficient four-wave mixing, Photonics **8**, 161 (2021).

[31] J. S. Levy, A. Gondarenko, A. C. Turner-Foster, M. A. Foster, A. L. Gaeta, and M. Lipson, in *2009 Conference on Lasers and Electro-Optics and 2009 Conference on Quantum Electronics and Laser Science Conference* (IEEE, Baltimore, Maryland, 2009), p. 1.

[32] A. Arbabi and L. L. Goddard, Measurements of the refractive indices and thermo-optic coefficients of Si_3N_4 and SiO_x using microring resonances, Opt. Lett. **38**, 3878 (2013).

[33] Vijay, S. Sharma, V. Venkataraman, and J. Ghosh, SiN waveguides for ultra-broadband visible-telecom photon pairs, Opt. Quantum Electron. **55**, 582 (2023).

[34] L. Wang, C. Hong, and S. Friberg, Generation of correlated photons via four-wave mixing in optical fibres, J. Opt. B: Quantum Semiclass. Opt. **3**, 346 (2001).

[35] S. Sharma, V. Kumar, P. Rawat, J. Ghosh, and V. Venkataraman, Nanowaveguide designs in 220-nm SOI for

ultra-broadband FWM at telecom wavelengths, IEEE J. Quantum Electron. **56**, 1 (2020).

[36] K. Garay-Palmett, H. McGuinness, O. Cohen, J. Lundeen, R. Rangel-Rojo, A. U'ren, M. Raymer, C. McKinstrie, S. Radic, and I. Walmsley, Photon pair-state preparation with tailored spectral properties by spontaneous four-wave mixing in photonic-crystal fiber, Opt. Express **15**, 14870 (2007).

[37] L. Zhang, C. Söller, O. Cohen, B. J. Smith, and I. A. Walmsley, Heralded generation of single photons in pure quantum states, J. Mod. Opt. **59**, 1525 (2012).

[38] P. J. Mosley, J. S. Lundeen, B. J. Smith, and I. A. Walmsley, Conditional preparation of single photons using parametric downconversion: A recipe for purity, New J. Phys. **10**, 093011 (2008).

[39] F. Graffitti, J. Kelly-Massicotte, A. Fedrizzi, and A. M. Brańczyk, Design considerations for high-purity heralded single-photon sources, Phys. Rev. A **98**, 053811 (2018).

[40] G. P. Agrawal, *Fiber-Optic Communication Systems* (John Wiley & Sons, Hoboken, New Jersey, 2012).

[41] M. Losurdo and K. Hingerl, *Ellipsometry at the Nanoscale* (Springer-Verlag, Berlin, 2013), Vol. 268.

[42] C. Vieu, F. Carcenac, A. Pepin, Y. Chen, M. Mejias, A. Lebib, L. Manin-Ferlazzo, L. Couraud, and H. Launois, Electron beam lithography: Resolution limits and applications, Appl. Surf. Sci. **164**, 111 (2000).

[43] J. Lugani, R. J. Francis-Jones, J. Boutari, and I. A. Walmsley, Spectrally pure single photons at telecommunications wavelengths using commercial birefringent optical fiber, Opt. Express **28**, 5147 (2020).

[44] R. Baets, A. Z. Subramanian, S. Clemmen, B. Kuyken, P. Bienstman, N. Le Thomas, G. Roelkens, D. Van Thourhout, P. Helin, and S. Severi, in *Optical Fiber Communication Conference* (Optica Publishing Group, Anaheim, California, 2016), pp. Th3J-1.

[45] L. G. Helt, Ph.D. thesis, Graduate Department of Physics, University of Toronto (2013).

[46] L. Helt, M. Steel, and J. Sipe, Spontaneous parametric downconversion in waveguides: What's loss got to do with it?, New J. Phys. **17**, 013055 (2015).

[47] S. Paesani, M. Borghi, S. Signorini, A. Maïnos, L. Pavesi, and A. Laing, Near-ideal spontaneous photon sources in silicon quantum photonics, Nat. Commun. **11**, 2505 (2020).

[48] W.-H. Cai, B. Wei, S. Wang, and R.-B. Jin, Counterpropagating spectrally uncorrelated biphotons at 1550 nm generated from periodically poled $M\mathrm{TiO}X\mathrm{O}_4$ ($M =$ K, Rb, Cs; $X =$ P, As), JOSA B **37**, 3048 (2020).

[49] Z. Ye, P. Zhao, K. Twayana, M. Karlsson, P. A. Andrekson, and V. Torres-Company, in *2021 Conference on Lasers and Electro-Optics (CLEO)* (IEEE, 2021), p. 1, https://www.proceedings.com/60677.html.

[50] J. F. Bauters, M. J. Heck, D. D. John, J. S. Barton, C. M. Bruinink, A. Leinse, R. G. Heideman, D. J. Blumenthal, and J. E. Bowers, Planar waveguides with less than 0.1 dB/m propagation loss fabricated with wafer bonding, Opt. Express **19**, 24090 (2011).

[51] D. J. Blumenthal, R. Heideman, D. Geuzebroek, A. Leinse, and C. Roeloffzen, Silicon nitride in silicon photonics, Proc. IEEE **106**, 2209 (2018).

[52] I. Kim, D. Lee, and K. J. Lee, Study of type II SPDC in lithium niobate for high spectral purity photon pair generation, Crystals **11**, 406 (2021).

[53] P. Vergyris, F. Kaiser, E. Gouzien, G. Sauder, T. Lunghi, and S. Tanzilli, Fully guided-wave photon pair source for quantum applications, Quantum Sci. Technol. **2**, 024007 (2017).